AIAA JOURNAL
Vol. 48, No. 9, September 2010

Flapping Wing Structural Deformation and Thrust Correlation Study with Flexible Membrane Wings

Pin Wu* and Peter Ifju†
University of Florida, Gainesville, Florida 32611
and
Bret Stanford‡
U.S. Air Force Research Laboratory, Wright–Patterson Air Force Base, Ohio 45440

DOI: 10.2514/1.J050310

This experimental study investigates the relationship between flapping wing structure and the production of aerodynamic forces for micro air vehicle hovering flight by measuring full-field structural deformation and thrust generation. Results from four flexible micromembrane wings with different skeletal reinforcement demonstrate that wing compliance is crucial in thrust production: only certain modes of passive aeroelastic deformation allow the wing to effectively produce thrust. The experimental setup consists of a flapping mechanism with a single-degree-of-freedom rotary actuation up to 45 Hz at 70 deg stoke amplitude and with power measurement, a force and torque sensor that measures the lift and thrust, and a digital image correlation system that consists of four cameras capable of capturing the complete stroke kinematics and structural deformation. Several technical challenges related to the experimental testing of microflapping wings are resolved in this study: primarily, flapping wings less than 3 in. in length produce loads and deformations that are difficult to measure in an accurate and nonintrusive manner. Furthermore, the synchronization of the load measurement system, the vision-based wing deformation measurement system, and the flapping mechanism is demonstrated. Intensive data analyses are performed to extract useful information from the measurements in both air and vacuum.

Nomenclature

a	=	horizontal distance from the rocker base pin center to the reciprocator center, 5 mm
c	=	wing root chord length, 25 mm
d	=	length of the rocker bar, 16 mm
f	=	flapping frequency, Hz
i	=	vertical displacement of the reciprocator, mm
l	=	length of the push rod in the crank-slider mechanism, 50 mm
r	=	offset distance in the crank module, adjustable to change the flapping amplitude, 3 mm
s	=	number of samples per cycle
x, y, z	=	local coordinate system of the flapping wings, mm
α	=	flapping wing position angle, deg
α_{twist}	=	angle of twist at 83% span location away from the root, deg
ΔT	=	triggering time interval, s
θ	=	motor rotational angle, deg

I. Introduction

THIS work is concerned with identifying the relationship between passive flapping wing deformations and the concomitant aerodynamic force production. Unlike birds and bats that have muscles and skeletal joints to actively change their wing shape (wingspan, planform, camber, dihedral, etc.) during flight, insects fly with wings that have no active shape control. Seen in high-speed videos and documented by Ellington [1], the key element for insect flight is the thrust produced by the sweeping motion. Wing pronation and supination also play important roles in insects' flight and control, but these aspects are outside of the scope of this paper. The sweeping motion is mainly a back-and-forth fan movement with various wing tip traces. Here, to emphasize pure flapping motion, a test bed mechanism is designed and created to perform a single degree-of-freedom (DOF) kinematics. This is categorized as normal mode hovering flapping flight with constant pitch angle, as illustrated by Shyy et al. [2]. Such kinematics are not typically considered to be biologically inspired [3], and the flapping of a rigid wing will probably not develop significant time-averaged lift/thrust. Wing flexibility then, becomes an important factor.

Recent interest in micro air vehicle (MAV) research has been directed toward the design of efficient flapping wing aircraft capable of both forward flight and hover. As MAVs usually have a wingspan less 150 mm and weigh less than 50 g, many challenges exist in terms of power, control, payload, etc., along with the most fundamental challenge of all: an effective wing with realizable kinematics to mimic nature's highly evolved flight mode. A firm understanding of the structural properties needed for an actuated wing to create effective aeroelastic forces is expected to be an enabling factor for the widespread use of flapping MAVs for a wide range of applications within the purview of aeronautical engineering and is the focus of this work.

Ho et al. [3] performed a similar study to understand flapping wing structures and aerodynamic behavior. They tested flapping membrane wing structures with and without batten reinforcement at the trailing edge of the wing tip as a function of advance ratio (composed of forward flight speed, total flapping angle, wingspan, and flapping frequency; essentially, this metric is used to estimate flow unsteadiness). For large values, the lift capabilities of the two wings are identical, but as the unsteady features of the flow are enhanced (low advance ratio), the wing without this reinforcement is inferior. The authors state that the excessive feathering (change of chord angle related to flow direction) of the wing disrupts the leading-edge vortex and the associated lift. Thrust, however, relies heavily upon wing flexibility for its development, and so an adequate compromise must be found. Singh et al. [4] also demonstrated this concept for a membrane wing with an unconstrained trailing edge, for which the feathering motion develops significantly more thrust force than one

Received 22 October 2009; accepted 6 January 2010.

*Research Assistant, Department of Mechanical and Aerospace Engineering; diccidwp@ufl.edu. Member AIAA.
†Professor, Department of Mechanical and Aerospace Engineering. Member AIAA.
‡National Research Council Postdoctoral Associate. Member AIAA.

reinforced all along its perimeter. Neither of these studies is able to provide quantitative experimental information concerning passive wing deformation. In general, relatively few publications exist in the area of experimental characterization of full-scale MAV wings (under 75 mm in length, flapped at over 25 Hz).

Because hummingbirds behave in the transition region between insect flight and bird flight, they are used as an example for the current flapping MAV development. Wu et al. [5] studied wings with a planform and size very similar to those of hummingbirds. Experimental characterization of such wings is challenging, as scaling must preserve many parameters: Reynolds number, Strouhal number, reduced frequency, and several flexibility parameters [2]. Because of these difficulties, it is desirable to conduct tests on full-scale models, leading to resolution issues in load measurements; time-averaged lift and thrust may only be a few grams. A wide range of measurement techniques can be found in the literature: Jones et al. [6] measured the displacement of a flapping MAV suspended by cables to estimate the thrust, whereas the use of wake-deficit information via particle image velocimetry aft of the flapping wing has also been demonstrated [7]; the accuracy of both of these techniques may suffer has the size of the wing decreases, however.

Singh and Chopra [4] mounted piezoresistive strain gauges to the wing joint to measure the aerodynamic forces. Such a method is attractive in that the (potentially large) inertial forces of the flapping mechanism are bypassed, but assumptions must be made as to the location along the wing where the mean aerodynamic force acts, and several substantial manufacturing issues are present, as discussed in their paper. This work uses a commercial force/torque sensor with 6 degrees of freedom (similar to the model used by Khan and Agrawal [8]) mounted beneath the flapping mechanism, as discussed in Sec. III.D. Furthermore, several subsystems (flapping mechanism, load sensor, strobe, cameras, etc.) must be synchronized within the flapping cycle, which requires a complex triggering system.

Because of the lightweight, fragile nature of the membrane wings, the candidate techniques for the measurement of flapping wing kinematics and structural deformation are necessarily limited to noncontact vision-based methods. Some work on this topic is found in the literature based upon pointwise techniques. For kinematics measurements, Raney and Slominski [9] placed small light-emitting diode devices at the wing tip and captured the entire wing tip trail in a single image. For deformation measurements, Tian et al. [10] used similar multiple reflective markers on a bat wing and stereo high-speed cameras to quantify the motion. Wallace et al. [11] and Agrawal and Agrawal [12] used a similar photogrammetry technique for insect-sized wings. A more full-field strategy is discussed by Zeng et al. [13], in which a fringe shadow method is used to measure the flapping and torsional angle of a dragonfly wing. Similar fringe-based methods are given by Wang et al. [14], along with sign points placed on the wing, to measure deformation of a free-flight dragonfly. Cheng et al. [15] extended this technique with a windowed Fourier transform to process the fringe patterns and extract phase. A method known as digital image correlation (DIC) [16] is used to measure the wing deformation in this work; the technique is generally regarded as state of the art in terms of experimental mechanics in general [17] and is particularly well suited to the flapping wing problem, due to its full-field, three-dimensional, high-resolution nature.

The remainder of this paper is organized as follows. First, the flapping mechanism and the four tested wings are introduced. Then the experimental setup is described in detail, including a vacuum chamber, a four-camera digital image correlation system, overall system trigger/synchronization and the force measurement system. The experimental procedure and data analysis are then presented, including a measurement uncertainty discussion. Finally, results are given to reveal the intrinsic relationship between wing deformation and aerodynamic performance.

II. Flapping Mechanism and Tested Wings

A single-DOF flapping mechanism is designed and created for this study, as shown in Fig. 1. The design is based on a Maxon motor system that includes a 15 W brushless dc motor EC16, a 57/13 reduction ratio planetary gear box, a 256 counts-per-turn encoder and an EPOS (model series code) 24 controller. This system provides precise control: the sensor provides position and velocity feedback to the controller that actively regulates the motor using a proportional–integral–derivative (PID) controller. The encoder also provides power consumption feedback so that energy efficiency can be calculated. Using a single rotational input for flapping allows for the use of the high-precision preassembled planetary gear head rather than constructing a custom gear transmission. The final output range of the motor shaft is of speeds from 0 to 45 revolutions per second (rps) and a nominal torque up to 21 N · m. In this work, data are taken

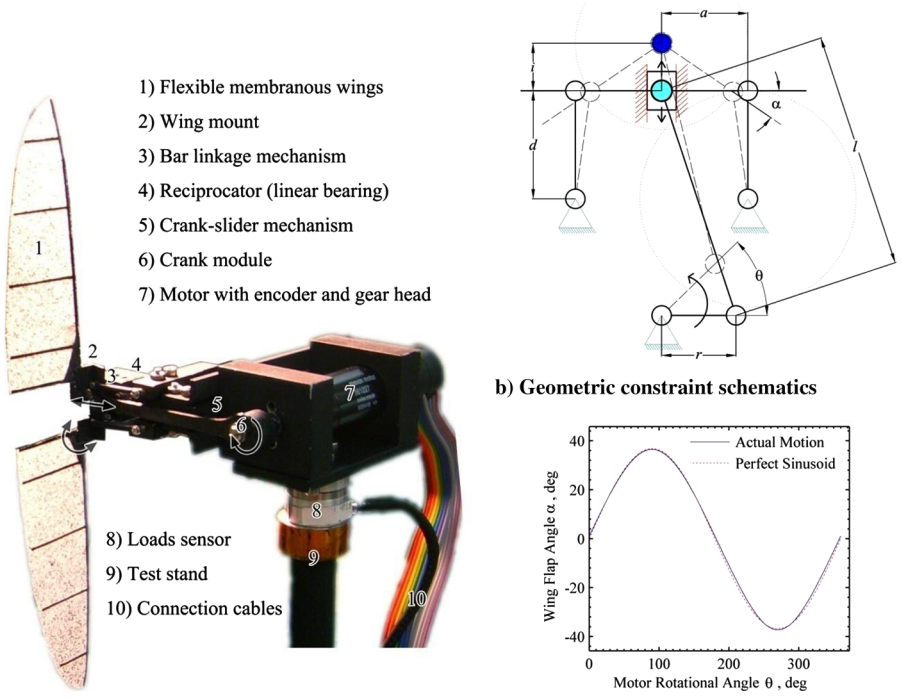

a) Flapping mechanism, 1DOF, +/-35 deg, 0~45 Hz

b) Geometric constraint schematics

c) Kinematics

Fig. 1 A single-DOF flapping mechanism: a) wings, motor, and loads sensor; b) constraint diagram; and c) resulting kinematics profile.

with flapping frequencies varying from 5 to 35 Hz at ±35 deg amplitude of the flap angle (α). The rotation input from the motor is first transformed into a reciprocating motion with a crank-slider mechanism; then a bar linkage mechanism realizes the flapping motion at the wing mount. A detailed schematic description of the flapping kinematics is presented in Fig. 1a. The geometric relationship between motor rotation (angle θ) and flap angle α is expressed as follows. For the crank-slider mechanism,

$$i = r\sin\theta + \sqrt{l^2 - r^2} - \sqrt{l^2 - r^2\cos^2\theta} \tag{1}$$

For the bar linkage mechanism,

$$i = a\sin\alpha + d\left(1 - \sqrt{1 - \frac{(1-\cos\alpha)^2 a^2}{d^2}}\right) \tag{2}$$

where i is the vertical displacement from the center point defined at the horizontal wing position ($\alpha = 0$). Using the values given in the Nomenclature, the selected parameters result in the near-sinusoidal kinematics profile seen in Fig. 1c.

All four wings tested are of a Zimmerman planform, formed by two ellipses that intersect at the quarter-chord. This wing planform is selected to have comparable geometric features with real hummingbird wings [18], with an aspect ratio of 7.65, a 75 mm wing length and a 25 mm root chord, as shown in Fig. 2. For this work, the wing design is two dimensional, with no camber or airfoil profile. The wings are constructed with unidirectional carbon fiber to form the skeleton and Capran® as the membrane. The carbon fiber skeletal reinforcement differs substantially for the four wings, which is reflected in the naming convention. The first wing is reinforced with batten oriented parallel to the root (battens parallel, BP), the second has radial diagonal battens similar to the feathering structures of a hummingbird wing (HUM), the third has no batten reinforcement other than the leading edge (leading edge only, LEO), and the final wing has carbon fiber reinforcement along the entire perimeter (perimeter reinforced, PR).

To manufacture the wing skeleton, a three-layer bidirectional carbon fiber triangular plate is first placed at the intersection of the leading edge and wing root, which can be used as an attachment point for other structure elements. This triangle is significantly stiffer than the remainder of the wing; therefore, it is used as a reference for deformation calculations (discussed in Sec. IV.B) and as an attachment location to the flapping mechanism (as seen in Fig. 1). Unidirectional carbon fiber strips (0.8 mm wide) are used to construct the leading edge, battens, wing root, and the trailing edge (only for PR). The strips are laid up on a flat plate according to each reinforcement pattern; the number of layers used for each portion of the wing is documented in Table 1. BP has two complete leading-edge layers and an additional layer between the root and the third batten (counting from the root), achieving a varying bending stiffness along the structure [19]. The other three wings all have two layers at the leading edge. All the battens are one layer and all the roots are two layers.

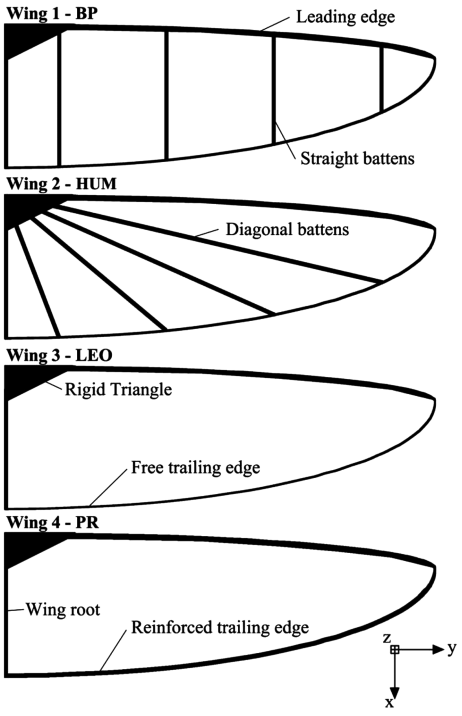

Fig. 2 Reinforcement layout of the four tested wings.

Table 1 Number of carbon fiber layers used in each portion of the wings, as well as the final reinforcement weight

	BP	HUM	LEO	PR
Leading edge	2 + 1 additional	2	2	2
Batten	1	1	0	0
Root	2	2	2	2
Trailing edge	0	0	0	1
Weight	0.125 g	0.150 g	0.100 g	0.140 g

After the carbon fiber skeleton is cured, the piece is applied with spray glue and laminated to a membrane material called Capran® (Honeywell's Capran Matt 1200), a biaxially oriented nylon film. Unlike the soft and deteriorative latex rubber, Capran® is as light as Mylar® (density: 1.16 g/cm^3), as tough as Tyvek® (tensile strength at break: 193–276 MPa), and as consistent as Kapton® (thermal shrinkage coefficient: 1–2% at 160°C). This thin film is available in matt finish (diffusive), making it amenable for DIC measurements. Its low-heat-shrink coefficient also allows the film to be cured together with the carbon fiber without building up excessive thermal stresses. Its high elastic modulus (2.5–3.4 GPa) and tear-resistant properties eliminate concerns about reinforcing the trailing edge. Finally, random patterns of flat black speckles are sprayed onto the wings for DIC measurements (discussed in Sec. III.B).

III. Experimental Setup

The overall experimental setup is shown in Fig. 3. The system includes a vacuum chamber, a four-camera DIC system, a force and torque sensor, and a control system that synchronizes all the instruments. Instrument specifications and configurations are discussed in this section.

A. Vacuum Chamber

The vacuum chamber allows for the measurement of wing deformation caused solely by inertial loading, isolated from aerodynamic effects. A square aluminum base plate ($30 \times 30 \times 1$ in.^{3}) is used as the platform for all of the instrumentation and is outfitted with four outlets for the vacuum pump, vacuum gauge, release valve, and electric feedthrough. A half-inch-thick clear acrylic bell jar, with a 24 in. inner diameter and a 24 in. inner height, is placed on the base plate and encloses all equipment: digital image correlation cameras (described in Sec. III.B), the flapping mechanism and wings, and the force and torque sensor, as shown in Fig. 3. The bell jar is lifted up to 25 in. above the aluminum base plate to avoid airflow obstruction during the experiments, which are conducted in hover condition. Reflective material is also placed around the bell jar to diffuse and bounce the stroboscopic light source. An Edwards VB12 vacuum pump is used for this setup, which lets the system reach −29.5 in. Hg vacuum in 5 min.

B. Digital Image Correlation System

DIC is a well-developed noncontact full-field stereo-image measurement technique used in this work to capture wing kinematics and structural deformation. The system uses stereo triangulation to digitize a random speckling pattern on the measurement surface and, thus, compute its three-dimensional features. This is followed by a temporal matching process, in which the system tracks a subset of the speckling pattern and minimizes a cross-correlation function to

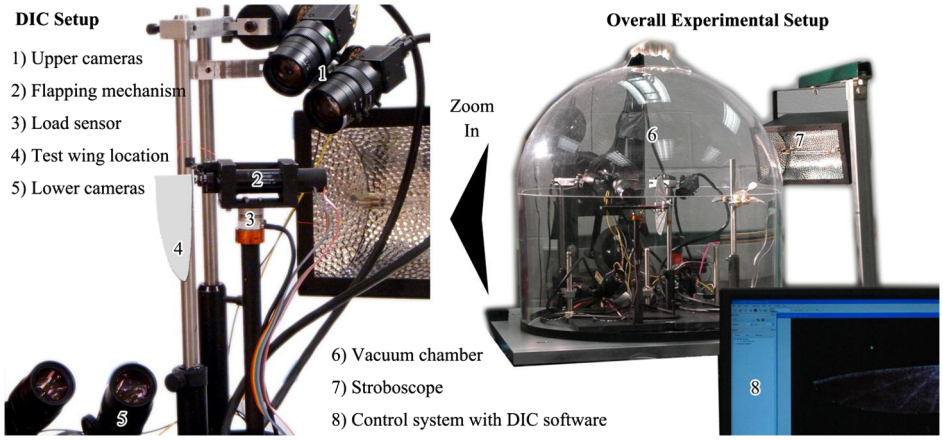

Fig. 3 Experimental setup.

compute the undeformed location of this subset and, thus, the displacements [16]. The correlation system consists of four Point Grey Research Flea2 cameras. Such a setup, after fine-tuning the depth of field, is able to capture the rigid body displacements (wing kinematics) and structural deformations of a single wing up to a ± 90 deg flapping amplitude. The upper pair camera system monitors the upper half-stroke and the lower pair the lower half-stroke. The four cameras are synchronized internally with an output to trigger a stroboscope for the lighting. Because the camera and stroboscope comprise a low-speed system (sampling rate lower than 10 frames per second), the kinematics and deformation sequences are generated by recording aliased image sequences (triggering at a progressing moment in each repeating cycle), similar to what can be taken with a high-speed system (sampling rate over thousands frames per second), given that there is no cycle-to-cycle variation.

The Flea2 cameras have 1/1.8 in. progressive scan charge-coupled devices with a 1624×1224 pixel resolution; a high-resolution speckle pattern can be applied for superior correlation. Their $29 \times 29 \times 30$ mm^3 dimension allows the cameras to fit inside the vacuum chamber. The multiple Flea2 cameras networked on the same IEEE-1394 bus are automatically synchronized to within a maximum deviation of 125 μs and equipped with triggering signal output. Computar's 12–36 mm F2.8 lenses are chosen for the Flea2 cameras. This combination gives the cameras a field of view between 22 and 61 deg. Careful selection of each camera parameter is crucial to obtaining a satisfactory depth of field. For example, a 95.2 mm depth of field results from a 0.25 m object distance and a 20 mm focal length, shot at F/16 aperture, with the circle of confusion defined as 20 μ for speckle recognition. The zoom lenses provide a certain degree of flexibility in positioning the cameras, and their continuous iris aperture helps to adjust for the desired depth of field.

The cameras are positioned and configured so that even large wing twist and bending can be captured, and there is enough depth of field to obtain sharp enough images during the whole flapping cycle. The cameras are not placed symmetrical to the test wing, as shown in Fig. 3. The upper pair of cameras is responsible for the upper half-stroke including passive wing twist, and so the cameras are positioned symmetrical to a plane that is normal to the wing surface at an expected angle (flap angle: 35 deg, twist angle: 22.5 deg) and in a plane that is normal to the wing surface at half the upper flapping angle (flap angle: 17.5 deg, twist angle: 0 deg). The lower pair of cameras takes images of the lower half-stroke and is positioned in the same way. After positioning the cameras, camera parameters are adjusted: focal length, focus, gain, and aperture. First the aperture is maximized and the focal length is adjusted so that the wing fills the field of view when the wing area appears to be maximal. Then the wing is moved to a flap angle of ± 17.5 deg and the foci of both pairs of cameras are adjusted. Once the focal plane is defined, the aperture is minimized (closed). Then all camera gain values are adjusted to the midpoint of the available range (in this case, 9.96 dB). The stroboscope is activated after this step. Then the aperture of each camera is opened so that the image has reasonable contrast between the base paint and the black speckles. The aperture is kept as small as possible to obtain the sufficient depth of field. The cameras are then calibrated with a grid pattern that fills the field of view, comparable to the wing size. The calibration grid is placed to imitate four wing locations for each camera pair: midplane without rotation, midplane with maximum rotation, the end of each stroke without rotation, and the end of each stroke with rotation. This step also double-checks all previous parameters. Finally, a reference image is taken when the wing is placed at the midplane (in a vertical position so that no deformation is caused by gravity). This reference image is taken for both camera pairs and is later used to unify the data in postprocessing.

C. System Synchronization Trigger

The instrument configuration and trigger timing determination are now discussed. The peak continuous sampling rate of the four cameras is 7.5 Hz. To capture flapping motion up to 35 Hz, correct triggering time is required so that a sequence of images at all flapping angles can be captured. High-speed cameras are not necessarily a superior alternative because of lighting requirements and difficulties of fitting the system into the vacuum chamber. For the current work, a linear stroboscope (Checkline LS-10-6000), triggered together with the shutter of the cameras, bursts an 8–10 μs pulse of light onto the flapping wings. The energy of each flash is 0.72 J with 1960 Lux illumination. This short flash duration freezes the flapping motion with a dark background (no motion blur tested up to 35 Hz). Mirrors and sheets of reflective material are used to direct the emitted light onto the wings to obtain more efficient illumination. By using the 9-pin 1394b interface to control all attributes of the cameras, registry values that control exposure, triggering modes, and strobe signal output can be modified. The cameras are set to high gain values according to the aperture value that gives a reasonable depth of field. This high gain setting drastically enhances the picture contrast, while also allowing additional noise that has a negligible effect upon the image correlation analysis. To reproduce a sequence of images that simulates what could be captured with high-speed videography, it is assumed that the wing deformation at different flapping frequencies and amplitudes should be time periodic. Because each data point is taken from a different cycle, only when periodicity is maintained will the phase loop form a smooth and differentiable shape (this will be confirmed to be true later with similar deformation phase plots shown in Fig. 7). Other high-frequency content caused by structural vibration is out of the scope of this study, although it is observed in some cases in a vacuum. The time interval between each trigger is determined by the following relationship: $\Delta T = (N + 1/s)/f$, where ΔT is the trigger time interval, s is the number of samples per cycle, f is the flapping frequency at steady state, and N is the number of complete cycles between sequential triggers. Because of the low-speed system and data transfer rate constraints, ΔT needs to be greater than 300 ms.

D. Nano17 Force and Torque Sensor

A force and torque sensor is used to measure the aerodynamic forces produced by the wings. The sensor needs to be able to measure at high sampling rates and have a high resolution for small forces; therefore, an industrial sensor Nano17 from ATI Automation, Inc. is selected, as shown in Fig. 3. Its measurement resolution is $1/320$ N (0.319 g) in both the thrust (F_x) and the lift (F_y) directions, which is adequate for the current application. The sensor's wire-cut high-yield-strength steel allows it to be overloaded 4.4 times its rated capacity before being damaged, though in this experiment the maximum possible loading condition is substantially below its rated capacity. The built-in silicon strain gauges provide a signal 75 times stronger than conventional foil gauges. This signal is amplified, resulting in near-zero noise distortion. The system, along with the associated 16-bit DAQ system by National Instruments, is calibrated to SI-12-0.12. In this study the sensor is used to measure the average thrust produced by the wings in air.

There are structural vibrations of the mechanism that should be taken into account in the loading history, as the sensor is not directly positioned at the wings; but such vibrations should not affect the average value, which is used to assess the wings' aerodynamic performance. This is because structural vibration within a system will not result in any net forces to the external environment when the displacement is zero. The flapping mechanism, attached only to the sensor, is not capable of applying an averaged nonzero external load. The only possible means of conducting net loading force to the sensor is through aerodynamics. Therefore, the structural vibration will not affect the average thrust value measured.

IV. Experimental Procedure and Data Analysis

A. Experimental Procedure

A flow chart is shown in Fig. 4 to illustrate the experimental procedure that includes control/input, operation, data acquisition, and data analysis. The experiment requires three control inputs: flapping frequency (5–35 Hz), the number of samples per flapping cycle (500 in this study) in the load measurements, and the time interval between triggers (300–450 ms) for the DIC cameras and stroboscope. The first two inputs are given to a virtual instrument (VI) program created for this experiment. The ΔT input is given to commercial software called VIC-Snap, which generates calibration correlation files and sends out trigger signals to the cameras.

The VI graphic user interface consists of two modules: one that communicates to the EPOS serial controller of the flapping mechanism, and the other that communicates to the data acquisition (DAQ) box of the Nano17. In the first module, the program establishes communication parameters and has the motor controller standing by. One can command position, velocity, and acceleration to the motor. At this stage, PID gains have already been tuned for operation. The information is stored in the EPOS controller and is called out by the VI. The PID control is performed by the EPOS controller and does not require resources from the VI. The VI controls input values to the EPOS controller and synchronizes with the other module. This module also records the electric current consumed by the motor, which is later converted to average power. In the second module, the VI specifies the sampling rate and number of samples per measurement to the Nano17 DAQ box. A constant number of samples per flapping cycle is first specified by the user (500 in this case), then the sampling frequency is calculated as the product of the flapping frequency and samples per cycle. Both of the modules allow users to store the motor feedback data and load measurements into text files. Only two components of the forces are recorded, corresponding to the thrust and lift.

In this study, the wings are actuated from 5 to 35 Hz (the highest frequency for each of the four wings varies because of different structures). In all cases the wings start at the same initial position. The operation sequence is as follows. After the user has defined a flapping frequency, sample number, and time interval, the VI control loop starts and establishes communication with the EPOS controller and Nano17. The DIC cameras are then initiated, taking pictures at the calculated frequency. The cameras control the stroboscope by a pulse signal generated with camera shutter actuation. Immediately, a trigger button is pressed in the VI to activate the flapping mechanism and load sensor. From the initial position, the wings accelerate at 2000 rpm/s to reach the command flapping frequency. The mechanism then stays at that frequency until the measurement is completed. In the mean time, the power used by the flapping mechanism is documented. About 40–100 cycles of load measurement data are taken in each run, and three separate runs of data are taken for calculating system errors. Three cycles of deformation measurements are recorded and there are about 50 frames of pictures in each cycle. This is done for each frequency and in both air and vacuum. This procedure outputs the text files for load measurements and .tif files for DIC measurements. Converting these raw files into data is discussed in Sec. IV.B.

B. Data Acquisition and Postprocessing

The load measurement text file output from the VI contains a data array, in which each row is the measurement for one flapping cycle. Because 500 samples are taken in each flapping cycle, there are 500 columns in the array (the sampling rate is altered along with the flapping frequency, that is, at 10 Hz, 5000 samples per second, and at 30 Hz, 15,000 samples per second). Usually 40–120 rows of data are taken for averaging. Because of random delays occurring at the hardware interface (for example, the time delay at reading from the computer memory buffer), each cycle recording is slightly shifted (phase delay); therefore, the data are shifted back before the averaging filter is applied. An example for this procedure is shown in Fig. 5. The instantaneous data taken for one cycle at 37.5 Hz of LEO are seen in Fig. 5a, with a significant level of measurement noise. In Fig. 5b, the ensemble averaged data over 60 continuous cycles are

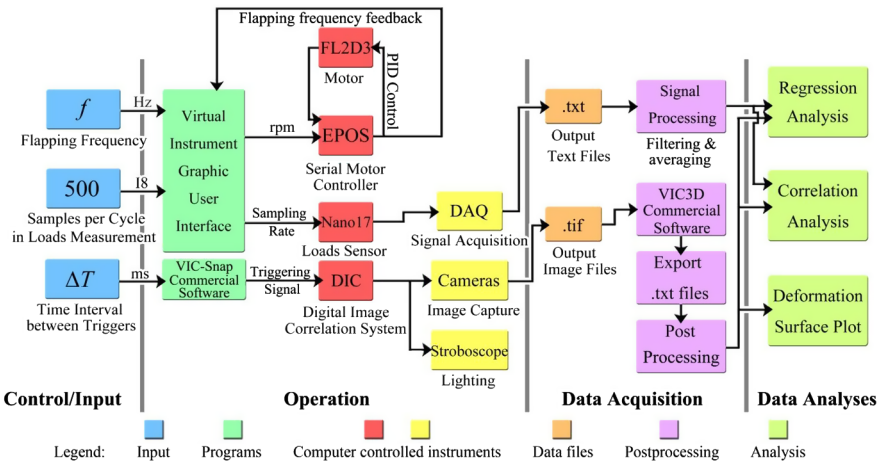

Fig. 4 Experimental procedure flow chart.

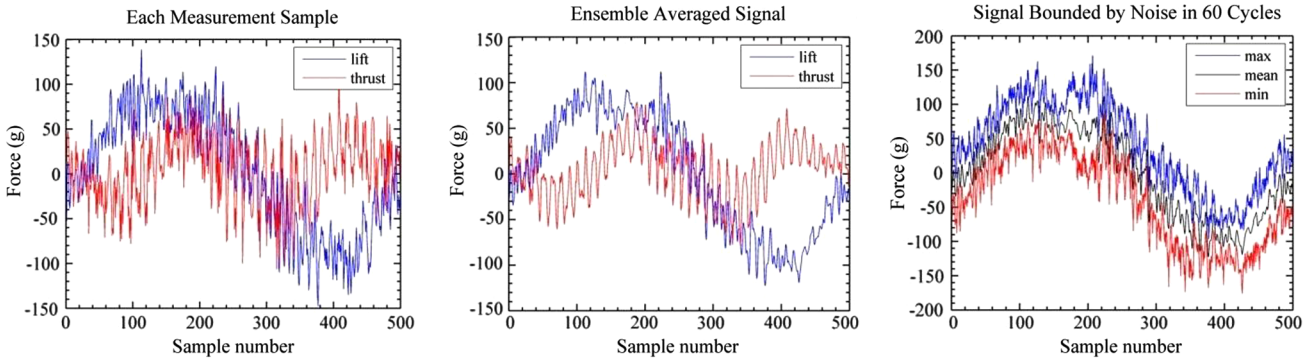

Fig. 5 Loads measurement postprocessing and system noise (LEO at 37.5 Hz in air).

shown, with a high-frequency vibration content (45 peaks per cycle, flapping frequency independent) observed. This vibration is thought to be the impact force at the contact of the teeth in the gear box. The shape of the waveform of the lower frequency is as expected: two peaks and two valleys are present in one flapping cycle, corresponding to thrust peaks during both the upstroke and the downstroke (symmetric motion). Figure 5c shows the maximum and minimum noise of the lift data taken from all 60 cycles, indicating the system noise level. A sinusoidal pattern is observed from the lift data, which is because the aerodynamic lift is combined with the inertial force generated by the flapping mechanism (the reciprocator, Fig. 1). Because of the symmetrical flapping motion, the average value for the lift is always zero. Therefore, in this study, because the kinematics is performed in hovering condition, only the time-averaged thrust is computed for each frequency and used for the following data analysis. The analysis conducted in Fig. 5 allows the user to evaluate the measurement characteristics of the system: what the random noise level is, how the noise can be reduced, and what maximum deviated values are present. This not only gives the user more confidence in the averaged values, but also allows for future application to logging data for cyclic loading history.

The .tif files are processed with commercial software VIC3D provided by Correlated Solution, Inc. The program correlates each pair of images and outputs the coordinates of data points on the wing surface into text files. These coordinates are computed relative to a reference image, which is given by the midplane of the flapping stroke at time zero. As discussed earlier, this reference image, taken of the static wing at midplane, is captured by both pairs of cameras. Based upon the position/orientation of each camera, various calibration parameters, and the orientation of the static wing with respect to each camera, the reference coordinate system established by each pair of cameras cannot be expected to coincide. Care must be taken, then, to stitch the two systems together, so that the flapping profile remains smooth as the data transitions from one camera system to the other, as shown in Fig. 6a. This is done by rotating both sets of reference data such that the static wing lies parallel to the x–y plane, and the leading edge is tangential to the y axis at the root. A separate transformation matrix is then available for each camera system. Next, each pair of wings is translated such that the wing root coincides with the x axis and the leading edge with the y axis. A separate displacement vector is then available for each camera system. Each image of the dynamic flapping wing captured with the upper pair of cameras is then rotated with the transformation matrix and translated with the displacement vector corresponding to the upper pair of cameras. A similar process is undertaken with the lower pair of cameras. Figure 6a also shows the undeformed wing at the upstroke and downstroke ends. Having stitched the two systems together, the DIC data can be used to compute the kinematic parameters.

VIC3D then generates the displacements of the wings at other positions during flapping. The displacements are composed of both rigid body motions (kinematics) and structural deformations. It is desirable to separate the two: the latter is much smaller than the former, but is expected to be the sole source of lift and thrust. For the test bed mechanism in this study, single-DOF flapping of a rigid wing does not produce time-averaged loads, but passive feathering of the trailing edge will. As such, the flexible wings designed and built in this work are very compliant to provide a large amount of bending and twisting. The rigid body motions and local surface deformations are separated by creating a fictitious undeformed wing surface at the same flapping angle as the deformed wing measured during flapping. The reference wing profile is transformed to match with the deformed profile at the rigid triangle base (Fig. 6b). This is done by first selecting three data points on the rigid triangle base. They are very close to one another and very close to the leading edge of the wing root. As these points are located close to the wing joint, it is assumed that their motion follows the rigid body kinematics without elastic deformation. The displacement data for each flapping image can then be used to find the new coordinates of these three data points throughout the stroke. For each flapping image, local coordinate

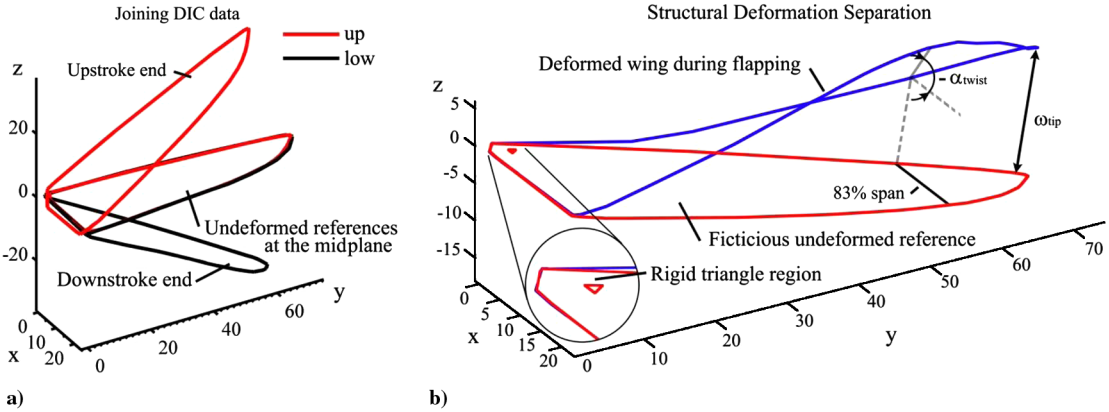

Fig. 6 Deformation measurement postprocessing.

systems are computed for the two pairs of triplets (one set that remains stationary at the midplane, and one that travels with the wing), and the rotational transformation matrix is subsequently computed. The static wing at midplane is then appropriately rotated and translated so that the two triplets coincide. The difference between the fictitious rigid surface and the elastic wing provides the sought-after structural deformations, indicated by ω in Fig. 6b. Two parameters describing the wing deformation are extracted from the data: the tip deflection ω_{tip} (wing bending, in millimeters), and the angle of twist α_{twist} (measured at 83% of the wing length). The positive sign of the angle of twist is defined as the angle formed when the trailing edge is below the leading edge.

C. Data Analysis

As stated earlier, the experiment is designed to obtain a relationship between the thrust production and the related structural deformation of flapping wings, as the wing compliance is the sole source for generating aerodynamic thrust. Three raw data types have been collected: average thrust, power consumption, and the full-field deformation. For the first data type, it alone can indicate the aerodynamic performance of the wings, though thrust coefficient can also be derived. The power consumption is converted into efficiency using the metric gram per watt (g/W), evaluating the thrust generated for each unit of power input. The full-field deformation has been represented with tip deflection and wing twist angle: the tip deflection tells the amount of wing bending (spanwise stiffness) and the twist angle describes the torsional compliance (or chordwise stiffness) of the wing. These two values are functions of flap angle, as illustrated in Fig. 7. This is because the full-field data cannot be directly used for further analysis; therefore, these two parameters are selected as abstraction, indicating, respectively, wing bending and twisting. Three example wings are selected from Wu et al. [20]; their stiffness varies from weak (example 1) to strong (example 3), and all are actuated at 25 Hz. In Fig. 7a, the phase loops go in counterclockwise direction; in Fig. 7b, they go clockwise.

The phase loops formed by the three wings enclose different areas and are oriented at different phase angles due to differences in their structural composition. The phase angle is defined as the angle between the line formed by the maximum and minimum y values (tip deflection) and the x axis, as shown in Fig. 7a. Example 2 produces the most thrust and it encloses the largest area in both tip deflection and wing twist, with an orientation that largely follows the commanded kinematics. The other two examples are inferior in thrust production: example 1 is too compliant to follow the kinematics, resulting in a phase angle larger than 90 deg, and example 3 is too stiff, enclosing very small loop areas. Therefore, two scalars can be used to represent the wing compliance: the loop enclosed area and phase angle. The processed data sheet contains the following information: flapping frequency, average thrust, net energy efficiency, total energy efficiency, tip deflection loop area in air and its phase, angle of twist area in air and its phase, tip deflection loop area in the vacuum and its phase, and angle of twist area in the vacuum and its phase. Correlation analyses can then be used to find statistical relationships among these values.

Table 2 Measurement uncertainties

Experimental result values	Uncertainties of 95% confidence	Number of samples used
Average thrust, g	±1%	60
Efficiency, g/W	±8%	20
Loop area, deg·mm or deg^2	±6%	3 cycles of data
Phase angle, deg	±12%	3 cycles of data

D. Measurement Uncertainties

The measurement uncertainties of each experiment are listed in Table 2. It should be noted that the absolute uncertainty values changes as the experiment parameter varies; therefore, the uncertainty value is presented by a rounded percentage. The errors of DIC are induced during the calibration phase and the uncertainty will remain the same after calibration. If a camera pair is carefully calibrated, the system uncertainty is under ±0.1 mm in the current setup (except that the speckle pattern occasionally introduces additional errors). However, the tip deflection and angle of twist data involve more than just DIC measurements: flapping mechanism precision, wing response, and density of data points in a loop would also change the extracted area and angle values. Also, because it is a low-speed system, the number of samples for calculating the uncertainty is limited to using discrete data.

V. Results

A. Wing Performance

In hovering conditions, flapping wing performance is evaluated with the effectiveness and efficiency in producing thrust. The average thrust produced by the four wings is shown in Fig. 8. The results clearly show that different wing structures lead to different performance. At a low-frequency range (below 25 Hz), PR and LEO have superior performance because of larger passive deformation: PR has a significant amount of mass distributed along the trailing edge and LEO has no reinforcement. At a higher-frequency range (above 25 Hz), the stronger reinforcement of BP and HUM yield higher thrust values; similar trends have also been reported in previous studies [20]. It should also be noted that, in all four cases, a portion of the frequency range provides a nearly linear increase in the thrust. An additional case of BP flapping in vacuum is also shown for comparison and confirmation that the wing inertia and mechanism actuation has no effect on average loads measurement. The average thrust measured in the absence of air is always near zero, with errors below the sensor resolution 0.32 g.

However, wing effectiveness cannot represent overall performance, because a wing that requires a higher frequency to achieve high thrusting forces may be inefficient [2]. Therefore, their net and overall efficiencies are compared in Fig. 9. The total efficiency is calculated from the ratio of thrust and total power; the net efficiency uses the ratio of thrust to the difference between the total power and the power needed to flap the wing in vacuum (therefore, the power consumed by the system's rotary inertia is removed in the net

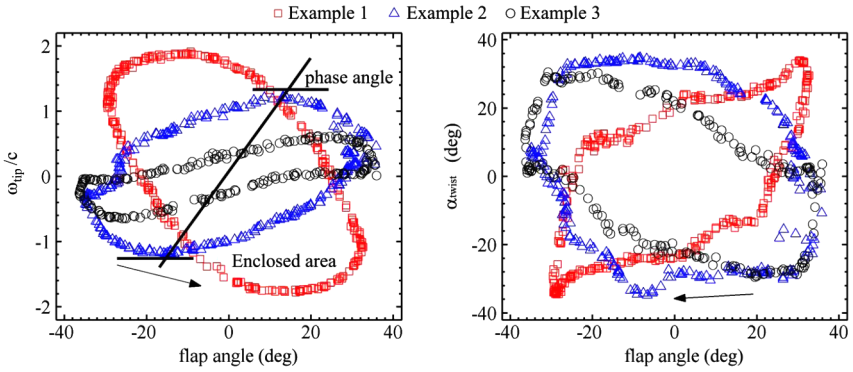

Fig. 7 Structural deformation data analysis.

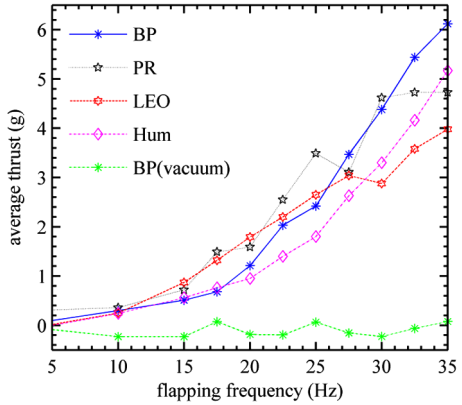

Fig. 8 Average thrust (g) of the four differently reinforced membrane wings.

efficiency calculation). It can be seen that LEO is the most efficient of the four for the majority of the presented frequency ranges. Because LEO is not reinforced with extra carbon fiber battens, it has the lightest weight (Table 1) and, therefore, the least power consumed for wing actuation. This also allows the wing to deform in an excessive manner (discussed later in reference to Fig. 11), which can be beneficial at a certain frequency range. Under the same reasoning, PR has significant mass distributed along the trailing edge (also the heaviest), requiring more energy for actuation and decreasing the efficiency. Combined with Fig. 8, PR's deformation patterns due to this inertial load produces the most thrust between 17.5 and 30 Hz. BP and HUM have more batten reinforcement, which constrains the wing deformation and reduces the thrusting efficiency. The net efficiency data are not plotted for 5 and 10 Hz because the measurement resolution is not high enough to differentiate the input power differences, causing overestimation.

B. Structural Deformation

1. *Effect of Frequency*

Higher flapping frequency corresponds to stronger inertial and aerodynamic loads imparted on the flapping wings, resulting in larger passive wing deformation. Figure 10 shows BP's structural deformation under actuation frequencies from 5 to 35 Hz. Figure 10a shows five selected frames during the downstroke for each frequency. The color contour represents the out-of-plane deformation normalized to the root chord length, which ranges from −1 to 1. The fictitious reference plane is plotted with solid gray lines to indicate the rigid body kinematics. It can be seen that the full-field DIC technique has captured all the relevant details of the structural deformation: inertial forces that cause the tip of the wing to snap at

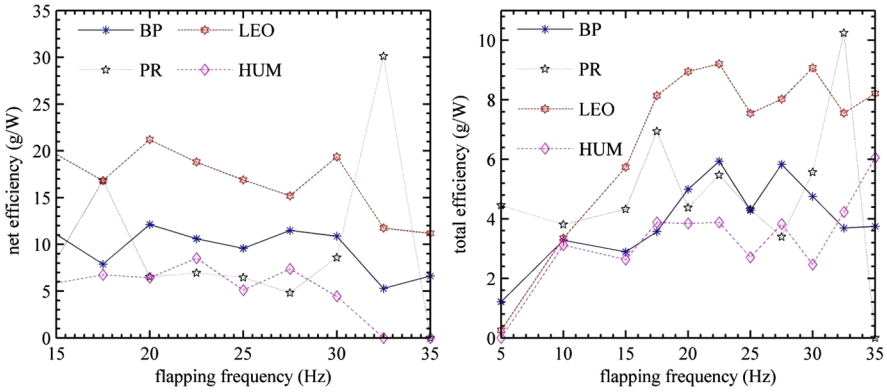

Fig. 9 Net and total efficiencies (g/W) of the four differently reinforced membrane wings.

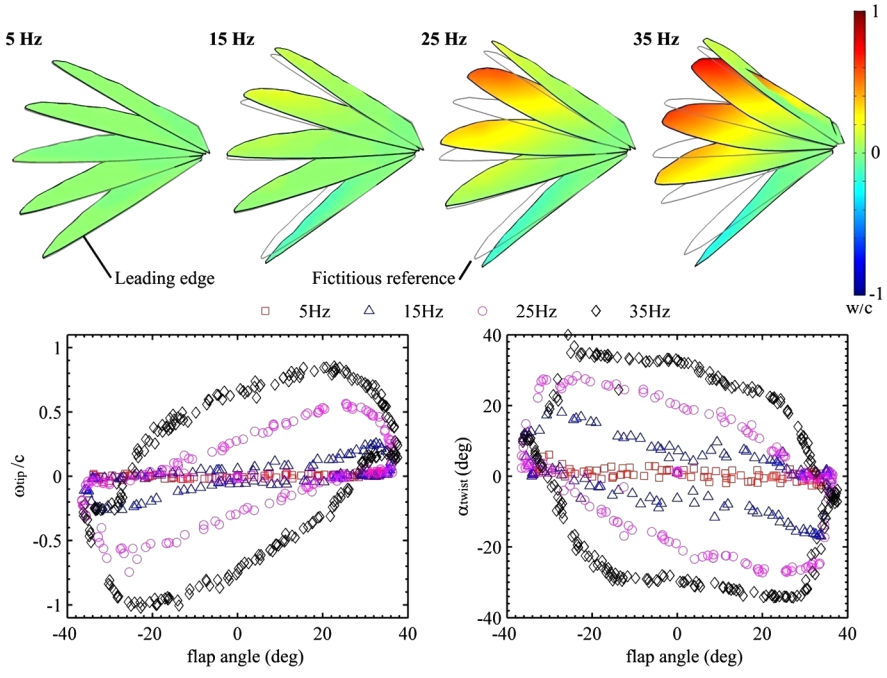

Fig. 10 BP structural deformation at different frequencies: a) contour plots through the downstroke, b) cyclic tip displacement, and c) cyclic wing twist.

stroke reversal (where the acceleration of the commanded kinematics are highest) and significant washout (wing twist) caused by aerodynamic loading near the midplane (where the wing velocity is highest). The complete cyclic deformation history is depicted with ω_{tip}/c and α_{twist} in Figs. 10b and 10c. It can be seen that, at 5 Hz, the wing experiences no significant deformation (also shown in the contour plots). As the flapping frequency increases, the area enclosed by the loops as well as the phase angles increases. Compared to Fig. 8, the increase in the passive wing deformation is well correlated to the increase of the average thrust produced by this wing. The small structural asymmetry (i.e., slightly different behavior through the upstroke as compared to the downstroke) is due to the one-sided membrane lamination and can be seen in the deformation phase loops, especially in the bending case shown in Fig. 10b.

Figure 11 shows LEO's structural deformation under frequencies from 15 to 22.5 Hz. The color contour scale in Fig. 11a now ranges from −1.5 to 1.5: larger deformation is observed compared to BP, even in a lower frequency range. This is because BP has a higher bending stiffness due to an extra layer of leading-edge reinforcement (Table 1). Furthermore, LEO's lack of batten reinforcement also allows for excessive membrane deformation. In Fig. 11b, the relationship between tip deflection and flap angle is similar to the data plotted earlier for BP, with a gradual increase in the area and phase of the loop with increasing frequency. The twist behavior shown in Fig. 11c, however, is distinctly different: even at lower frequencies, the wing twist is very large, reaching the peak value of 40 deg seen over the entire test matrix (BP is also constrained by this limit, as seen in Fig. 10). Higher frequencies do not substantially alter the twisting amplitude, though the location in the flapping stroke where this maximum occurs is shifted. Such behavior would indicate an extremely nonlinear wing structure (presumably due to the lack of batten reinforcement) wherein fairly small forces cause exaggerated deformations, though increased actuation provides little additional deformation (hardening). LEO's inability to alter its twist profile during the frequency sweep probably causes the aforementioned linear relationship between thrust and frequency seen in Fig. 8 (output airflow is proportional to flapping frequency). This shows that the passive deformation pattern of Fig. 11 does not significantly contribute to obtain extra thrust, unlike with BP (Fig. 10), where wing deformation patterns correspond to a parabolic increase in thrust production. This result would indicate that wings with excessive flexibility may not be ideal to achieve high thrust, even though they are very efficient.

2. *Effect of Structure*

At the same flapping frequency, different wing structures would generate different thrust with unique deformation patterns. Figure 12 shows the four wings' deformation patterns at 20 Hz. As already mentioned, Fig. 12a shows the full-field deformation through the downstroke: tip-snap magnitude is indicative of the wing bending stiffness as well as the mass distribution. BP has the stiffest leading edge and, therefore, deforms the least at the tip, though the large mass distribution along the trailing edge (and the concomitant inertial forces) must be thought of as the reason why PR has the largest bending deformation. The radial battens of HUM provide some reinforcement in the span direction, resulting in the least deformation of all the two-layer leading-edge wings. LEO, as noted earlier, has the largest wing twist because of the absence of batten reinforcement.

Referring to Fig. 8, LEO produces the most thrust, PR the second, BP the third, and HUM the least at a frequency of 20 Hz. The deformation history shown in Figs. 12b and 12c matches with this thrust result very well: LEO encloses the largest loop area in both plots and has the largest amount of wing twist; therefore, it has the most thrust. BP, however, encloses smaller areas than HUM while producing more thrust, which indicates that the phase angle may play a more important role: HUM is more flexible, producing tip deflection peaks much later after wing reversal. Between a −15 and 15 deg flap angle, the area difference in the angle of twist loops does not benefit additional flow in the thrust direction, even if passive wing twist is a good indicator of fluid/structure interaction. There may be extra airflow generated but scattered to other (nonthrusting) directions [19]. These correlation trends will be further discussed in Sec. V.C.

3. *Effect of Aeroelastic Coupling*

When the experiment is conducted in vacuum, wing deformation is purely caused by inertial loadings, as shown in Fig. 13. A direct comparison with the results given earlier (in air) should provide insight into the separate roles of inertial and aerodynamic loading, as well as aeroelastic coupling effects. The amplitude of the tip snap seen at stroke reversal is similar in Figs. 10 and 13, which would indicate that aerodynamic loading plays a minimal role in this behavior, as expected. The most immediate result from Fig. 13 is that, for all of the frequencies tested, the wing twist through the midstroke (0 deg flap angle) is nearly zero. This is to be expected, as the angular acceleration (and, hence, the inertial forces) should be zero through

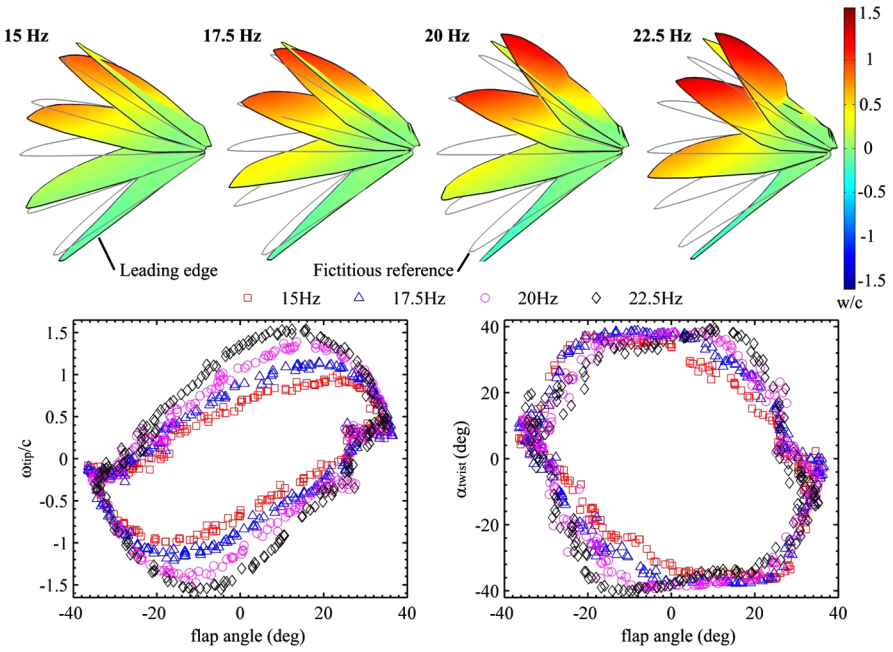

Fig. 11 LEO structural deformation at different frequencies: a) contour plots through the downstroke, b) cyclic tip displacement, and c) cyclic wing twist.

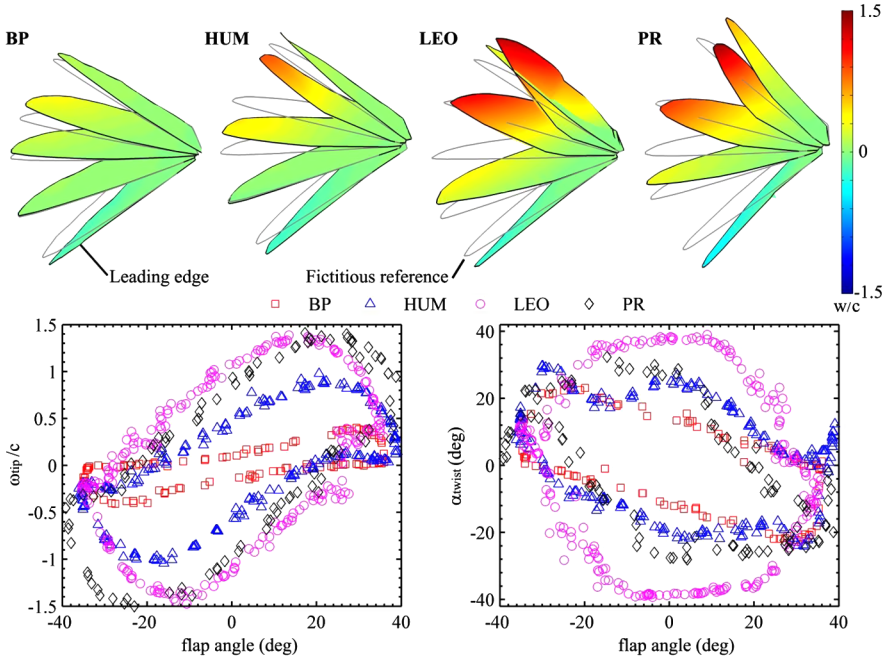

Fig. 12 Structural deformation for all four wings at 20 Hz: a) contour plots through the downstroke, b) cyclic tip displacement, and c) cyclic wing twist.

the midstroke for the sinusoidal flapping considered here. This is in direct contrast to the large twisting seen in Fig. 10, which is almost solely due to aerodynamic loading (which will be maximum through the midstroke, during which the angular velocity is peak). This behavior causes the twist and tip deflection phase loops to collapse at the origin of the plots, and the area enclosed by the loops is much smaller than seen in the air data of Fig. 10.

The wing stiffness, therefore, dictates how large the phase loop will form in vacuum. As flapping frequency increases, inertial loads increase quadratically and the response time for the wing tip to recover after the snap becomes longer, forming the loop seen in the 25 Hz case. At the highest frequency of 35 Hz, each tip snap becomes a mechanism to transform kinetic energy into elastic potential energy: the wing is elastically bent like a loaded spring. In the absence of air damping, the tip trajectory overshoots its kinematic route near the midstroke plane and forms a third loop. It can also be seen that the vacuum environment exaggerates the asymmetrical properties of the wing (i.e., the membrane skin is bonded to the upper portion of the carbon fiber skeleton): bending stiffness is smaller through the upstroke, providing a larger loop.

C. Thrust and Deformation Correlation

Given that all the four pairs of wings are actuated under exactly the same conditions (kinematics, frequency, Reynolds number, and environment), the cause for the disparate thrust (Fig. 8) and efficiency (Fig. 9) measurements is completely due to the differences in wing structure. Such differences are captured with the full-field

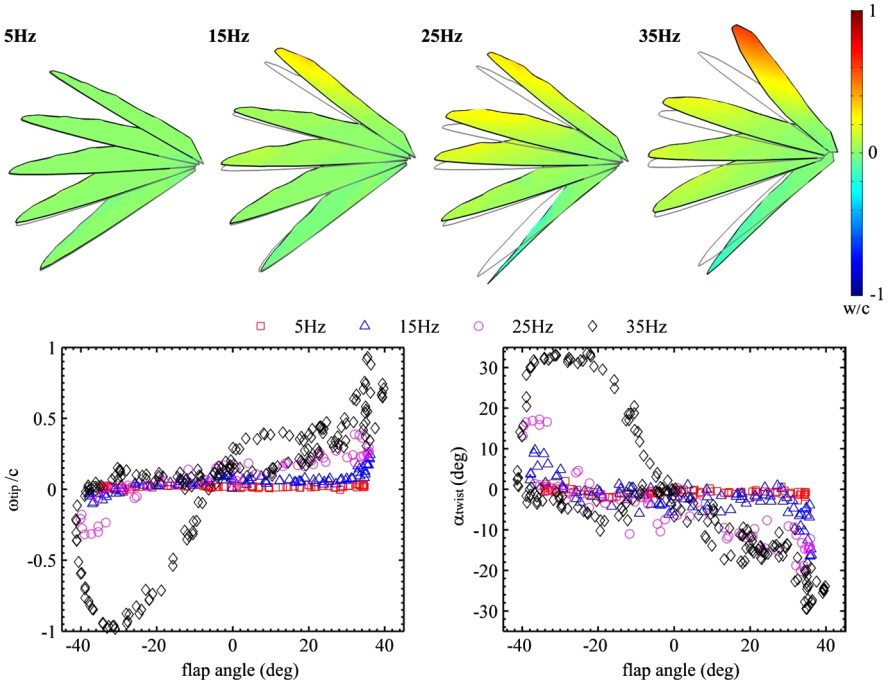

Fig. 13 BP at different frequencies in vacuum: a) contour plots through the downstroke, b) cyclic tip displacement, and c) cyclic wing twist.

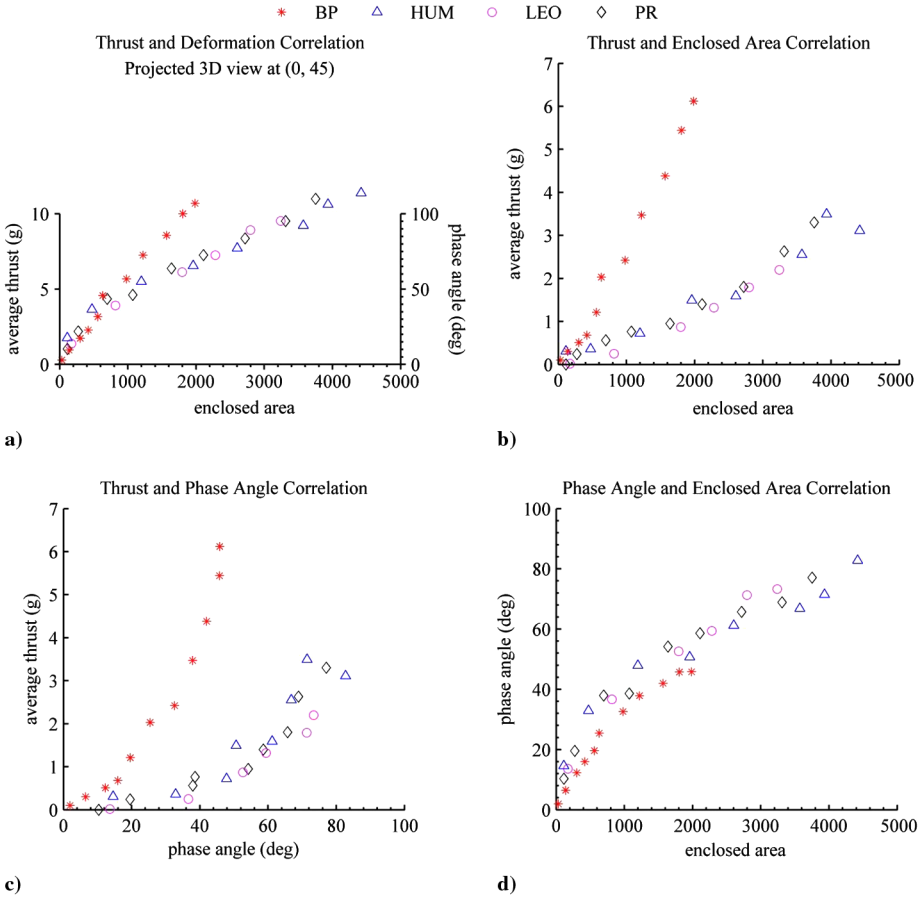

Fig. 14 Correlation between average thrust and wing tip deformation.

DIC measurements and expressed in two key parameters: tip deflection for bending and twist angle for feathering, as shown in Fig. 6. The statistical correlation between such parameters and the average thrust value may reveal certain trends, which in turn can provide a general set of design strategies for the aeroelastic tailoring of flexible flapping wings. Figure 14 shows the correlation results between thrust and tip deflection, the latter of which is converted into the area enclosed by the phase loops (deg ·mm) and the loop phase angle that describes how much the actual motion (of the wing tip, for example) is lagging behind the commanded actuation. Figure 14a shows the relationships of all four wings between the three variables: area, phase angle, and thrust, viewed at 0 deg azimuth angle and 45 deg elevation angle. Data from BP form a linear trend line, fitting onto a plane out of page; so do the other three wings'. This means the trend lines are bending-stiffness specific: the HUM, LEO, and PR wings have the same leading-edge structure (Table 1) and, therefore, similar bending stiffness, collapsing into the same trend line. It is important to realize that in this figure the trend lines are independent of flapping frequency (which is the only kinematic variable in this study), which indicates that the plot relates wing structure directly to aerodynamic performance. Similarly, Figs. 14b and 14c show the two trend lines that reflect how the bending stiffness affects wing deformation during flapping and the thrust generated by such deformation. In Fig. 14c, however, it is interesting to notice that, at the last two data points, BP reaches a maximum phase angle while the enclosed area linearly increases with thrust.

Finally, Fig. 14d provides a result that ignores the aerodynamic thrust production: the relationship between the enclosed area and phase angle. In Figs. 14a–14c, two trend lines are formed distinctly because of the different leading-edge stiffness. Here, the data from all four wings nearly collapse to a single curve, showing a more general trend. This result suggests that a stiffer wing would enclose a smaller area while the phase angle increases at a very similar rate to the more compliant wings. Presumably, such characteristics of BP allow the wing to produce the most thrust at high frequencies, comparable to the results presented by Wu et al. [20] for three-layer leading-edge wings.

VI. Conclusions

This paper has detailed the development of an experimental setup aimed at providing a relationship between wing structure and thrust generated by passive deformation of four micro flexible flapping wings. Each wing is constructed from a carbon fiber skeleton affixed with a thin membrane skin. The orientation and thickness of the discrete carbon fiber members has a substantial impact on the nature of the passive wing deformation (which is due to a complex combination of unsteady inertial and aerodynamic loading) and the concomitant thrust production. For this study, wings are actuated with a single-DOF rotary flapping motion: a rigid wing would generate little useful aerodynamic forces under such a motion, but the passive feathering, twisting, and bending of the membrane wings can provide meaningful thrust forces. The wing motion (which can be separated into rigid body motions and structural deformations) is measured with a high-resolution whole-field digital image correlation system, while a force-torque system is used to measure the average thrust and power efficiency over a flapping cycle.

This work has advanced the state of the art of flapping wing MAV research in many aspects and has added value to the less-noticed field of the study of flapping wing structure and its related performance. The experiments are conducted under strictly controlled parameters comparable to a hummingbird's flight: flapping frequency range, wing size, wing weight, and aerodynamic thrust. The application of DIC in this study, capturing the full-field structural deformation of the rapid moving wings in both air and vacuum, is pioneering. The postprocessing method developed based on these techniques allows further analysis and interpretation of the data. A correlation study shows clear trends that indicate the relationship between structural

stiffness and aerodynamic performance: with 1-DOF kinematics, 1) the chordwise stiffness needs to be orders of magnitude lower than the spanwise stiffness to achieve thrust effectiveness and efficiency, 2) the spanwise stiffness needs to be optimized based on a particular frequency range and wing inertia to be efficient, and 3) the deformation pattern created due to structural/aerodynamics coupling is what needs to be tailored to optimize performance. Different tests have been exhaustively performed to characterize the wing's structural properties and performance. Regarding the results of the tests, the following conclusions can be drawn:

1) Membrane wings with stronger skeletal reinforcement provide superior thrust at high frequencies (above 25 Hz); the opposite is true at lower frequencies. Thrust generally grows quadratically with flapping frequency, though extreme twisting deformations (e.g., seen by LEO) can limit this growth to a linear trend.

2) Passive wing deformation strongly governs the efficiency (ratio of thrust generation to power consumption). Nonbatten reinforcement, as in LEO, is found to be the most efficient over the majority of the tested frequency range. Wing mass and its distribution is another important factor affecting efficiency.

3) The effect of frequency, structure, and aeroelastic coupling are examined for wing deformation using color contour as well as phase-loop representations of the wing bending and twisting.

4) When flapping in air, the plot of wing tip deflection versus flapping angle forms a counterclockwise loop, whereas wing twist versus flapping angle forms a clockwise loop. This is because, as the wing travels through downstroke, aerodynamic forces press the wing upward and cause washout (negative twist). This twisting motion is thought to be a major contributor to the thrust development. At stroke reversal, the wing experiences a tip snap, which is solely due to the inertial forces.

5) When flapping in vacuum, wing deformation through the middle of each stroke is minimal (as the aerodynamic forces are zero), and so the phase loops collapse at the origin of the plots. Behavior at stroke reversal is largely unaffected.

6) Wings with adequate batten reinforcement (i.e., BP) show a monotonic growth in wing deformation with flapping frequency. In contrasting, largely unreinforced wings (LEO) have very large twisting motions at relatively low frequencies. The amplitude of this deformation remains relatively unchanged with increased actuation, which is indicative of strong hardening geometric nonlinearities within the structure.

7) The PR wing, which has a large amount of mass located along the outboard portions of the structure, generates the largest tip displacement at stroke reversal, whereas LEO, with no chordwise reinforcement, has the largest amount of wing twist.

8) There is a strong correlation between the thrust generation, the enclosed area, and the phase angle of the tip deformation phase loops. The intrinsic relationship between wing structure and its ability to produce thrust is represented in these trend lines, regardless of flapping frequency. The relationship between the two deformation parameters is also found to be irrelevant to the aerodynamic consequences.

Acknowledgments

The authors would like to thank the U.S. Air Force Office of Scientific Research for funding this project under MURI #69726, as well as Ron Brown and Michael Braddock for their help.

References

[1] Ellington, C., "The Aerodynamics of Hovering Insect Flight III. Kinematics," *Philosophical Transactions of the Royal Society of London Series B, Biological Sciences*, Vol. 305, No. 1122, 1984, pp. 41–78. doi:10.1098/rstb.1984.0051

[2] Shyy, W., Lian, Y., Tang, J., Viieru, D., and Liu, H., *Aerodynamics of Low Reynolds Number Flyers*, Cambridge Univ. Press, New York, 2008.

[3] Ho, S., Nassef, H., Pornsinsirirak, N., Tai, Y., and Ho, C., "Unsteady Aerodynamics and Flow Control for Flapping Wing Flyers," *Progress in Aerospace Sciences*, Vol. 39, No. 8, 2003, pp. 635–681. doi:10.1016/j.paerosci.2003.04.001

[4] Singh, B., and Chopra, I., "Insect-Based Hover-Capable Flapping Wings for Micro Air Vehicles: Experiments and Analysis," *AIAA Journal*, Vol. 46, No. 9, 2008, pp. 2115–2124. doi:10.2514/1.28192

[5] Wu, P., Stanford, B., Bowman, S., Schwartz, A., and Ifju, P., "Digital Image Correlation Techniques for Full-Field Displacement Measurements of Micro Air Vehicle Flapping Wings," *Experimental Techniques*, Vol. 33, No. 6, 2009. doi:10.1111/j.1747-1567.2008.00450.x

[6] Jones, K., Duggan, S., and Platzer, M., "Flapping-Wing Propulsion for a Micro Air Vehicle," AIAA Paper 2001-0126 , Jan. 2001.

[7] Parker, K., Soria, J., and Von Ellenrieder, K., "Thrust Measurements from a Finite-Span Flapping Wing," *AIAA Journal*, Vol. 45, No. 1, 2007, pp. 58–70. doi:10.2514/1.18217

[8] Khan, Z., and Agrawal, S., "Design and Optimization of a Biologically Inspired Flapping Mechanism for Flapping Wing Micro Air Vehicles," *IEEE International Conference on Robotics and Automation*, Inst. of Electrical and Electronics Engineers, New York, April 2007, pp. 373–378. doi:10.1109/ROBOT.2007.363815

[9] Raney, D., and Slominski, E., "Mechanization and Control Concepts for Biologically Inspired Micro Air Vehicles," *Journal of Aircraft*, Vol. 41, No. 6, 2004, pp. 1257–1265. doi:10.2514/1.5514

[10] Tian, X., Iriarte-Diaz, J., Middleton, K., Galvao, R., Israeli, E., Roemer, A., Sullivan, A., Song, A., Swartz, S., and Breuer, K., "Direct Measurements of the Kinematics and Dynamics of Bat Flight," *Bioinspiration & Biomimetics*, Vol. 1, No. 4, 2006, pp. S10–S18. doi:10.1088/1748-3182/1/4/S02

[11] Wallace, I., Lawson, N., Harvey, A., Jones, J., and Moore, A., "High-Speed Photogrammetry System for Measuring the Kinematics of Insect Wings," *Applied Optics*, Vol. 45, No. 17, 2006, pp. 4165–4173. doi:10.1364/AO.45.004165

[12] Agrawal, A., and Agrawal, S., "Design of Bio-Inspired Flexible Wings for Flapping-Wing Micro-Sized Air Vehicle Applications," *Advanced Robotics*, Vol. 23, No. 7, 2009, pp. 979–1002. doi:10.1163/156855309X443133

[13] Zeng, L., Matsumoto, H., and Kawachi, K., "A Fringe Shadow Method for Measuring Flapping Angle and Torsional Angle of a Dragonfly Wing," *Measurement Science and Technology*, Vol. 7, No. 5, 1996, pp. 776–781. doi:10.1088/0957-0233/7/5/009

[14] Wang, H., Zeng, L., and Yin, C., "Measuring the Body Position, Attitude and Wing Deformation of a Free-Flight Dragonfly by Combining a Comb Fringe Pattern with Sign Points on the Wing," *Measurement Science and Technology*, Vol. 13, No. 6, 2002, pp. 903–908. doi:10.1088/0957-0233/13/6/311

[15] Cheng, P., Hu, J., Zhang, G., Hou, L., Xu, B., and Wu, X., "Deformation Measurements of Dragonfly's Wing in Free Flight by Using Windowed Fourier Transform," *Optics and Lasers in Engineering*, Vol. 46, No. 2, 2008, pp. 157–161. doi:10.1016/j.optlaseng.2007.08.001

[16] Sutton, M., Turner, J., Bruck, H., and Chae, T., "Full Field Representation of the Discretely Sampled Surface Deformation for Displacement and Strain Analysis," *Experimental Mechanics*, Vol. 31, No. 2, 1991, pp. 168–177. doi:10.1007/BF02327571

[17] Orteu, J., "3-D Computer Vision in Experimental Mechanics," *Optics and Lasers in Engineering*, Vol. 47, No. 3, 2009, pp. 282–291. doi:10.1016/j.optlaseng.2007.11.009

[18] Altshuler, D., Dudley, R., and Ellington, C., "Aerodynamic Forces of Revolving Hummingbird Wings and Wing Models," *Journal of Zoology: Proceedings of the Zoological Society of London*, Vol. 264, 2004, pp. 327–332. doi:10.1017/S0952836904005813

[19] Wu, P., Stanford, B., and Ifju, P., "Passive Bending and Twisting Motion During the Flapping Stroke of a Micro Elastic Wing for Thrust Production," AIAA Paper 2009-879, Jan. 2009.

[20] Wu, P., Ifju, P., Stanford, B., Sällström, E., Ukeiley, L., Love, R., and Lind, R., "A Multidisciplinary Experimental Study of Flapping Wing Aeroelasticity in Thrust Production," AIAA Paper 2009-2413, May 2009.

F. Pai
Associate Editor